Two Stable Equilibria of the Atlantic Subpolar Gyre

ANDREAS BORN AND THOMAS F. STOCKER

Climate and Environmental Physics, Physics Institute, University of Bern,
and Oeschger Centre for Climate Change Research, Bern, Switzerland

(Manuscript received 25 March 2013, in final form 18 September 2013)

ABSTRACT

The cyclonic circulation of the Atlantic subpolar gyre is a key mechanism for North Atlantic climate variability on a wide range of time scales. It is generally accepted that it is driven by both cyclonic winds and buoyancy forcing, yet the individual importance and dynamical interactions of the two contributions remain unclear. The authors propose a simplified four-box model representing the convective basin of the Labrador Sea and its shallow and deep boundary current system, the western subpolar gyre. Convective heat loss drives a baroclinic flow of relatively light water around the dense center. Eddy salt flux from the boundary current to the center increases with a stronger circulation, favors the formation of dense waters, and thereby sustains a strong baroclinic flow, approximately 10%–25% of the total. In contrast, when the baroclinic flow is not active, surface waters may be too fresh to convect, and a buoyancy-driven circulation cannot develop. This situation corresponds to a second stable circulation mode. A hysteresis is found for variations in surface freshwater flux and the salinity of the near-surface boundary current. An analytical solution is presented and analyzed.

source: https://doi.org/10.48350/47327 | downloaded: 10.4.2024

1. Introduction

Decadal climate variability in the Atlantic Ocean and on neighboring continents is closely connected with variations in the subpolar gyre (SPG) (Häkkinen and Rhines 2004; Yoshimori et al. 2010; Yeager et al. 2012; Matei et al. 2012), and dynamic variations in the gyre's circulation play an active role in shaping this variability, with significant potential for decadal predictability (Delworth et al. 1993; Hátún et al. 2005; Spall 2008; Robson et al. 2012; Tulloch and Marshall 2012). This importance stems mainly from its influence on the Atlantic meridional overturning circulation (AMOC) (Hátún et al. 2005; Böning et al. 2006; Gao and Yu 2008; Rhein et al. 2011), but also owes to the fact that the horizontal gyre circulation dominates meridional heat transport in the subpolar latitudes of the Atlantic Ocean as well as projected changes thereof (Böning and Bryan 1996; Spall 2004; Yang and Saenko 2012).

Although the importance of its variability is beyond controversy, the origin of variations and response to atmospheric forcing is the subject of considerable debate. Several studies attribute a dominant role for the average circulation and variations to buoyancy fluxes (Lohmann et al. 2009a; Böning et al. 1996; Eden and Willebrand 2001; Curry and McCartney 2001) while others point to wind forcing as the source of variability (Böning et al. 2006; Häkkinen et al. 2011). However, the relative importance of both probably depends on the time scale considered, with the barotropic wind forcing acting faster (Eden and Willebrand 2001; Eden and Jung 2001; Langehaug et al. 2012). Besides the separation in the temporal domain, a regionalization of fluxes may provide further insight. It is clear that local atmospheric fluxes of buoyancy are the main driver for deep convection in the western basin (Marshall and Schott 1999; Yashayaev and Loder 2009; Våge et al. 2009), which creates lateral density gradients that drive a baroclinic circulation. In contrast, wind patterns to which the SPG responds strongly are located over the eastern part of the basin (Häkkinen et al. 2011; Langehaug et al. 2012; Condron and Renfrew 2012). Notwithstanding these simplifications, advective transport by the Irminger Current preconditions the central Labrador Sea's surface waters to lower the convective threshold. Thus, some yet undetermined degree of interaction exists between the wind- and buoyancy-driven circulations.

Corresponding author address: Andreas Born, University of Bern, Sidlerstrasse 5, 3012 Bern, Switzerland.
E-mail: born@climate.unibe.ch

DOI: 10.1175/JPO-D-13-073.1

© 2014 American Meteorological Society

Here, we present an idealized four-box model of the SPG to investigate and quantify its sensitivity to variations in atmospheric forcing and the water masses that reach the region with the prevailing currents. Up to one-quarter of its total transport is due to the surface buoyancy flux, forcing a baroclinic flow. However, it is suggested that this relatively small part plays an important role for variations of the circulation, including rapid changes. This is the result of a nonlinearity involving mutually increasing salt flux to the convective center of the Labrador Sea and the baroclinic flow around its rim. The same mechanism brings about a hysteresis of the SPG circulation with respect to surface freshwater flux or boundary current salinity, formally similar to well-known models of the AMOC (Stommel 1961; Marotzke 1990; Stocker and Wright 1991; Rahmstorf 1996; Marotzke 2000). The impact of the wind-driven circulation on the two stable modes of circulation is investigated as well as the sensitivity of the SPG to changes in the Greenland–Scotland Ridge overflow transport.

The idealized four-box model is presented in section 2. Results for equilibrium experiments and the sensitivity to various changes in boundary conditions are shown in section 3, followed by the analytical solution in section 4. We discuss the results in section 5 and summarize in section 6.

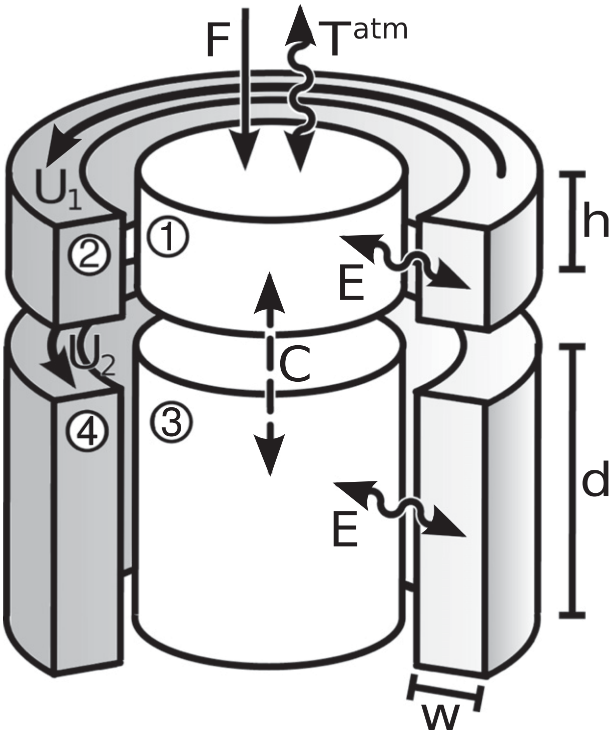

FIG. 1. Four-box model of the North Atlantic subpolar gyre. The U_1 and U_2 are the upper and lower boundary currents, F is the surface freshwater flux, and T^{atm} is the atmospheric temperature to which the upper ocean layer is relaxed. The letter C denotes parameterized convective mixing, and E denotes parameterized eddy fluxes of heat and salt.

2. Formulation of the model

The model domain consists of two cylindrical boxes representing a convective basin (Fig. 1) and two annular boxes for the upper- and intermediate-depth boundary currents that completely encircle the central basin. The upper two boxes represent the buoyant surface layer of the central Labrador Sea and the shallow boundary current, respectively. The lower two boxes are the convective basin and the intermediate-depth boundary current. This geometry is a common simplification that has been used in previous conceptual studies of the Labrador Sea (Straneo 2006b; Deshayes et al. 2009), but it is a good approximation also for more complex numerical setups (Spall 2004; Iovino et al. 2008) and the World Ocean Circulation Experiment Repeat section 7 (WOCE AR7) across the Labrador Sea (Marshall and Schott 1999; Straneo 2006a; Yashayaev 2007). The vertical separation between central and boundary boxes is at the same depth, 100 m. In the vertical dimension, the domain covers the upper 1500 m, which is loosely based on the depth of Labrador seawater in the boundary current (Straneo 2006b; Yashayaev 2007; Holliday et al. 2009). In years of strong convection, Labrador seawater does reach a greater depth in the central Labrador Sea basin and probably interacts with the deepest part of the boundary current consisting of Northeast Atlantic Deep Water and Denmark Strait overflow water. However, because these water masses are part of the deep western boundary current and do not usually recirculate in the subpolar North Atlantic, the dynamic effect of water masses below 1500 m is not considered here.

Atmospheric fluxes are only considered for the central basin, not the boundary current. This is motivated by the fact that the boundary current is relatively strong and narrow so that surface fluxes are comparatively small compared to advection within the ocean. Moreover, the upper boundary current is meant to represent the warm water core of the Irminger Current, which is not in direct contact with the surface because of very fresh and buoyant waters from the East Greenland Current. Further details on the configuration for the Labrador Sea are given below the description of the basic dynamics.

The model uses four prognostic variables, the temperatures and salinities of the central boxes 1 and 3. Temperature and salinity of the annular boxes 2 and 4 are held constant at values estimated from observations (see below).

a. Surface

Three processes change the temperature of the upper layer of the convective basin: relaxation to variable atmospheric temperatures, eddy heat exchange with the boundary current, and intermittent convection and mixing with box 3 below. Similarly, salinity changes are the result of a constant freshwater flux through the surface, lateral eddy salt flux from the boundary current, and convection.

While convection is treated separately, eddy mixing and air–sea fluxes are formalized as

$$\partial_t T_1 = cU_1(T_2 - T_1) + \tau^{-1}[T_0^{\text{atm}} - T_{\text{amp}}^{\text{atm}} \cos(\omega t) - T_1] \quad \text{and} \tag{1}$$

$$\partial_t S_1 = cU_1(S_2 - S_1) - F_S, \tag{2}$$

where ∂_t represents the time derivative, T_n and S_n are the temperature and salinity of box n, U_1 is the vertically averaged velocity of the upper boundary current, and c is the eddy mixing efficiency for which details are provided below. The terms T_0^{atm} and $T_{\text{amp}}^{\text{atm}}$ are the climatological surface air temperature and its seasonal amplitude, respectively. The seasonal cycle of atmospheric temperatures is approximated by a negative cosine function with angular frequency ω. The value τ is the time scale of relaxation of the surface waters to the surface air temperature, t is the time, and F_S is a virtual surface freshwater flux.

b. Middepth

Without direct contact to the surface, the tracer composition in the lower layer depends only on eddy mixing with the lower boundary current:

$$\partial_t T_3 = cU_2(T_4 - T_3) \quad \text{and} \tag{3}$$

$$\partial_t S_3 = cU_2(S_4 - S_3). \tag{4}$$

Here, U_2 is the depth-averaged velocity of the deep boundary current.

c. Convection

Convection is not part of the prognostic Eqs. (1)–(4) but is handled separately at each model time step. When the density of the upper water exceeds that of the deep water column, $\sigma_1 > \sigma_3$, the two volumes are mixed instantaneously and completely by taking the volume-weighted average of the two end members. Mixing with a relaxation time of up to 14 days yields results that are indistinguishable from the simple instantaneous mixing scheme and therefore will not be used. Density anomalies are calculated from a linearized equation of state:

$$\Delta\sigma = \beta\Delta S - \alpha\Delta T, \tag{5}$$

using the thermal and haline expansion coefficients α and β, respectively.

d. Velocity of the boundary current

The barotropic part of the velocity is an external parameter, assumed to be driven by winds and other driving factors that depend on regions outside the domain of the model and the effect of wind stress that is not explicitly simulated. This is based on recent findings that the SPG significantly covaries with the east Atlantic pattern (EAP), cyclonic wind anomalies over the eastern North Atlantic (Häkkinen et al. 2011; Langehaug et al. 2012). We derive an expression for the baroclinic part of the boundary current from the thermal wind equation, making use of the simplified geometry of the domain:

$$\partial_z u = -\frac{g}{f\rho_0}\partial_r \sigma, \tag{6}$$

$$\partial_r \sigma = \frac{\Delta\sigma}{w}, \tag{7}$$

$$\partial_z u = \frac{u_{\text{bcl}}}{h}, \quad \text{and} \tag{8}$$

$$u_{\text{bcl}} = -\frac{g}{f\rho_0}\frac{h}{w}\Delta\sigma, \tag{9}$$

where we used r as the across-stream (radial) coordinate and z as the vertical. The term u is the along-stream velocity, u_{bcl} is the integrated thermal wind at the top of the boundary current, g is the gravitational acceleration, ρ_0 is a reference density, and f is the Coriolis frequency at 55°N. The value w is the width of the boundary current, and h and $\Delta\sigma$ denote the height and density difference between the center and boundary current at each of the two levels.

The baroclinic velocities integrate from the bottom up, offset by the depth-independent barotropic velocity U_{btp}. Thus, the velocity of the deep and upper boundary current and the total volume transport are

$$U_2 = U_{\text{btp}} - \frac{gd}{2f\rho_0 w}(\sigma_4 - \sigma_3), \tag{10}$$

$$U_1 = U_2 - \frac{gh}{2f\rho_0 w}(\sigma_2 - \sigma_1), \quad \text{and} \tag{11}$$

$$M = U_1 wh + U_2 wd, \tag{12}$$

where h has been changed to d for the lower level. Note that a factor 0.5 has been introduced to the thermal wind part to account for linear shear over the layer thickness. The terms U_1 and U_2 are vertical averages of the velocities of their respective boxes.

e. *Estimate eddy flux efficiency*

Eddy heat transport across a narrow front is commonly described as

$$\overline{v'T'} = c^*U\Delta T, \tag{13}$$

where v' and T' are deviations from the temporal averages of cross-front velocity and temperature, multiplied and averaged over time as indicated by the overbar (Spall and Chapman 1998; Straneo 2006b; Spall 2012). The variable U is the alongfront (advective) velocity, ΔT is the temperature difference between both sides of the front, and c^* is a dimensionless mixing efficiency constant, not to be confused with c in Eqs. (1)–(4). The value of c^* is approximately 0.03 as determined from baroclinic instability theory and confirmed from laboratory and numerical experiments (Visbeck et al. 1996; Spall and Chapman 1998). Note that we use the total velocity U in Eq. (13) and thus apply the parameterization outside its theoretical rationale that includes only the baroclinic flow. This is motivated by the fact that the underlying baroclinic eddy diffusivity is proportional to the inverse Eady time scale (Green 1970; Stone 1972) that in turn describes the growth of baroclinic instabilities as linearly dependent on the velocity of the perpendicular current. The time scale of growth of barotropic instabilities (e.g., Kelvin–Helmholtz) also grows linearly with the advective shear velocity. Consequently, a parameterization of the form of Eq. (13) is qualitatively correct for both the barotropic and baroclinic components, although the parameter c might be different. An expression of c in terms of c^* is found by calculating the total heat flux across the front, from the boundary current into the central basin:

$$Q = \int_A \overline{v'T'}c_V\rho_0\, d\hat{A} = c^*U\Delta T c_V\rho_0 A, \tag{14}$$

with the specific heat capacity at constant volume c_V and the surface area between the boundary current and central basin A. This heat flux results in a warming of the central basin:

$$\partial_t T = \frac{Q}{c_V V\rho_0} = c^*\frac{A}{V}U\Delta T = cU\Delta T, \tag{15}$$

where V is the volume of the central basin. Equation (15) yields the eddy mixing efficiency c. It is formally equivalent to Eq. (13).

f. *Surface freshwater flux*

The freshwater flux through the surface F is converted into a salt flux F_S (virtual freshwater flux) by assuming a reference salinity S_0 and the depth of the upper central basin in which the freshwater is diluted:

$$F_S = F\frac{S_0}{h}. \tag{16}$$

MODEL CONFIGURATION AND BOUNDARY VALUES

The dimension of the model boxes approximates the Labrador Sea and its primary water masses. The radius of the central basin is 300 km, the width of the boundary current is 100 km. In the vertical dimension, upper and lower boxes are separated at a depth of 100 m. The upper level simulates the exchange between the Irminger Current and the surface of the central Labrador Sea. The lower level represents the exchange between the newly formed Labrador seawater and the water masses flowing around the basin at the intermediate depth.

Note that while the vertical separation at 100 m in the model is reasonable for the buoyant surface layer in the central Labrador Sea, it does not correspond to the depth of the Irminger Current that reaches several times that depth. This is a consequence of the spatially explicit discretization of the model that cannot take into account mixing along isopycnals. However, because of the strong isopycnal slopes in upper layers of the Labrador Sea, the surface of the central basin is indeed in contact with much deeper water masses in the boundary current. We take this into account by assigning the temperature and salinity of the Irminger Current to the upper boundary current of the model despite its unrealistic depth range.

The Irminger Current's water is the primary source of salt and heat in the region, with a relatively high salinity of 35 psu and a temperature of 10°C (Yashayaev 2007). The lower boundary current represents the water mass below the Irminger Current that mainly consists of Icelandic Slope Water. Icelandic Slope Water is a water mass resulting from the mixing of Iceland–Scotland overflow water and overlying Atlantic water, with a temperature of 4°C and a salinity of 34.9 psu (van Aken and de Boer 1995; Yashayaev 2007). It does not include Labrador seawater. The deeper water masses of Northeast Atlantic Deep Water and the very dense Denmark Strait overflow water are not represented in this model. They form an important part of the deep western boundary current and as such do not usually recirculate in the subpolar basins. Moreover, they are not in direct contact with the lighter Labrador seawater and hence do not contribute to dynamic changes in the region (Dickson and Brown 1994).

The average surface air temperature over the central Labrador Sea T_0^{atm} is 6°C with a seasonal amplitude $T_{\mathrm{amp}}^{\mathrm{atm}} = 8°\mathrm{C}$. Freshwater flux into the ocean is approximated as a constant flux of $1\,\mathrm{m\,yr^{-1}}$, which is higher than current estimates of net atmospheric fluxes (Walsh and Portis 1999; Myers et al. 2007), but also includes sea ice melting and runoff. Density variations are calculated in the model using the linear equation of state [Eq. (5)], approximated for the central Labrador Sea with a temperature of 5°C and a salinity of 34 psu. Thus, the thermal and haline expansion coefficients are $\alpha = 0.11\,\mathrm{kg\,m^{-3}\,K^{-1}}$ and $\beta = 0.77\,\mathrm{kg\,m^{-3}\,psu^{-1}}$, respectively. The barotropic volume transport is 20 Sverdrups (Sv; $1\,\mathrm{Sv} \equiv 10^6\,\mathrm{m^3\,s^{-1}}$), which for the chosen size of the boundary current, upper and lower, equates to a barotropic velocity of $U_{\mathrm{btp}} = 0.133\,\mathrm{m\,s^{-1}}$.

TABLE 1. List of default model parameters.

Constant	Value
r	300 km
w	100 km
h	100 m
d	1400 m
S_0	35 psu
ρ_0	$1026\,\mathrm{kg\,m^{-3}}$
c^*	0.03
f	$1.19 \times 10^{-4}\,\mathrm{s^{-1}}$
α	$0.11\,\mathrm{kg\,m^{-3}\,K^{-1}}$
β	$0.77\,\mathrm{kg\,m^{-3}\,psu^{-1}}$
τ	30 days
T_2	10°C
S_2	35 psu
T_4	4°C
S_4	34.9 psu
T_0^{atm}	6°C
$T_{\mathrm{amp}}^{\mathrm{atm}}$	8°C
ω	$2\pi\,(365\,\mathrm{days})^{-1}$
F	$1\,\mathrm{m\,yr^{-1}}$
U_{btp}	$0.133\,\mathrm{m\,s^{-1}}$

3. Results

a. Equilibrium dynamics and relaxation time

The model is forced with constant seasonal forcing similar to observations of recent climate (Table 1), expressed by time-varying surface air temperature as in Eq. (1). The temperature of the upper central basin closely follows the air temperature during times when convection does not occur (Fig. 2d). The temperature of the upper boundary current has little impact on the temperature of the central basin because the relaxation to surface air temperatures is about one order of magnitude stronger than the eddy heat exchange for typical values of U_1, that is, $\tau^{-1} \approx 10cU_1$ [cf. Eq. (1)]. Seasonal variations in salinity and density compare well with measurements from ocean weather ship Bravo, while water temperatures are too high in summer (Lazier 1980). However, warm summer temperatures do not adversely affect the dynamics of the model because they are limited to the upper central box in the absence of deep convection.

Temperatures and salinities of the two central basins are initialized with the same values as their corresponding boundary current so that density contrasts and baroclinic velocities are zero. Once in equilibrium, box 1 freshens during the warm season until convection sets in and saline waters from box 3 mix upward (Fig. 2c). The salinification of box 1 and freshening of box 3 corresponds to the ratio of the volumes of the two boxes, $1/14$. Deep convection and mixing continues throughout the cold season during which both reservoirs cool together and accumulate salt from both the upper and lower boundary currents. After temperatures in the upper central basin have risen sufficiently, convection stops again and boxes 1 and 3 disconnect. Temperature and salinity develop independently throughout the warm season. Without the convective flux of cold and freshwater from above, box 3 relaxes to the values of the deep boundary current, warmer and more saline waters. The temporal progression is conveniently summarized in a *T–S* diagram that at the same time is the phase space of the two pairs of prognostic variables (Fig. 3).

Volume transport in the boundary currents equals the barotropic transport of 20 Sv at the beginning of the simulation (Fig. 2a). After 3 yr of integration, the annual-average volume transport is within 0.5% of its equilibrium value of 25.9 Sv. Thus, a little less than one-quarter of the total transport is due to baroclinicity. The strengthening of the baroclinic circulation is mostly due to the increase in density in the lower central basin (Fig. 2b), caused by cooling while freshening counteracts (Figs. 2c,d). Density changes in the upper central basin do not significantly impact the circulation because of its shallow depth. Intra-annual variations in SPG transport with a standard deviation of 1.49 Sv (Fig. 2a) are primarily the result of density changes in the lower basin. The standard deviation of the upper-level transport is 0.23 Sv.

b. Sensitivity to local (F) and remote (S_2, S_4) freshwater forcing

Variations in volume transport of the boundary current are primarily the result of density changes in the

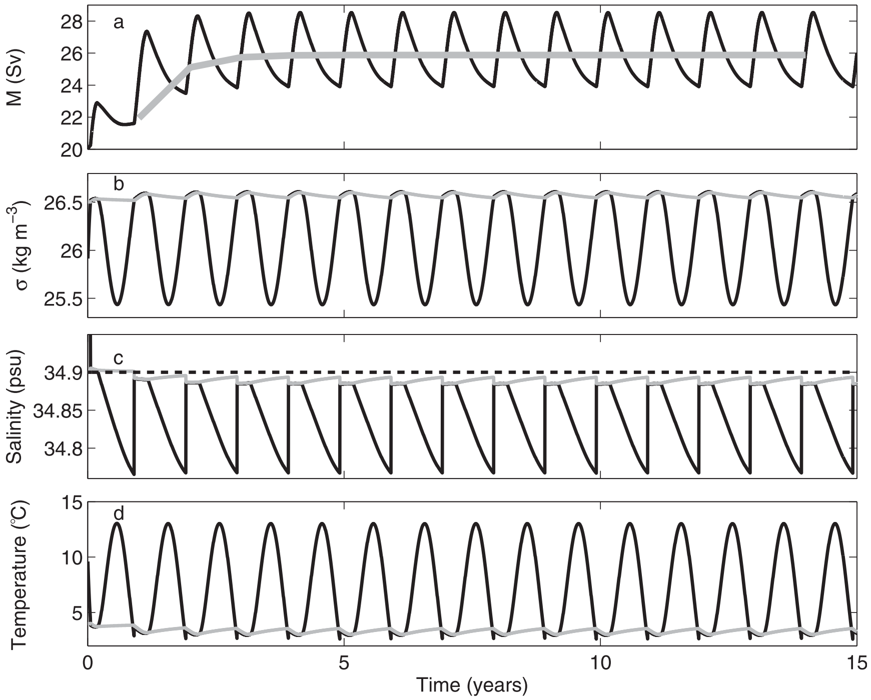

FIG. 2. Time evolution of key variables in the strong circulation mode. (a) Daily- (black) and annual-average (gray) transport *M* of the SPG. (b)–(d) Black (gray) lines denote values for box 1 (box 3). Dashed line in (c) is the salinity of the lower boundary current S_4.

lower central basin, which in turn are due to cooling by convective events. Convection is largely controlled by the density of the upper water mass that varies in response to the fixed seasonal cycle, surface freshwater flux, and the dynamic contribution of eddy exchange with the boundary current.

To investigate the response to changes in the freshwater balance, we vary the salinity of the upper boundary current S_2 and eddy salt transport into the convective basin (Fig. 4). The S_2 linearly decreased from 36 to 31 psu and back to 36 psu over a simulation time of about 2740 yr (10^6 time steps of 1-day duration), which is slow enough for the quickly responding model to remain in continuous quasi equilibrium. Between S_2 = 34.29 and 34.69 psu, two stable modes of circulation exist, one with active deep convection and a baroclinic contribution to the SPG circulation of about 2–5 Sv and one with only the prescribed barotropic circulation of 20 Sv.

This hysteresis is explained by a positive feedback involving eddy salt transport and the velocity of the boundary current. If the salinity of the upper boundary current is relatively high, eddy salt flux into the central basin is always strong enough for deep convection to occur. This then increases the density of the water column and maintains the baroclinic circulation. With decreasing salinity of the boundary current, the eddy salt flux is not large enough under all circumstances, but depends on the strength of the boundary current. If it is already strong, the circulation is able to sustain itself despite a relatively weak salinity difference. Because the baroclinic flow is a significant part of the boundary current velocity, the additional eddy salt flux it causes is important. Therefore, when the baroclinic circulation is not active, an important source of salt is missing for the upper central basin, making it less dense and thus raising the convective threshold. Below a certain level, the salinity of the boundary current is too low for even a strong baroclinic circulation to compensate its effect on eddy salt flux. In this case, convection and the baroclinic circulation fail.

The location of the hysteresis on the S_2 axis depends on the salinity of the lower boundary current S_4 because changes there indirectly impact the salinity of the upper central basin S_1 that enters the eddy salt flux term in the upper level [Eq. (2)]. The model's equations may be simplified to using only the salinity difference $S_2 - S_4$, in which case all curves in Fig. 4 will collapse onto one. It is intuitively clear that the width of the hysteresis is determined by the relative contribution of the baroclinic flow to the total. Thus, a weaker barotropic transport allows for the two stable regimes to spread over a broader range of salinities as will be shown below.

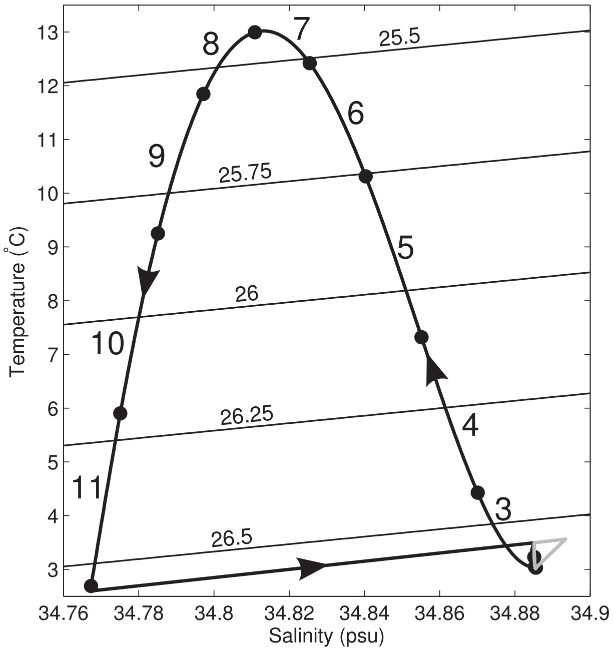

FIG. 3. Diagram of *T*–*S* for the time evolution of box 1 (black) and box 3 (gray), summarizing the four prognostic variables. Thin diagonal lines show isopycnals. Black dots mark the beginning of every month, which are numbered. The direction of trajectories is anticlockwise (black) and clockwise (gray).

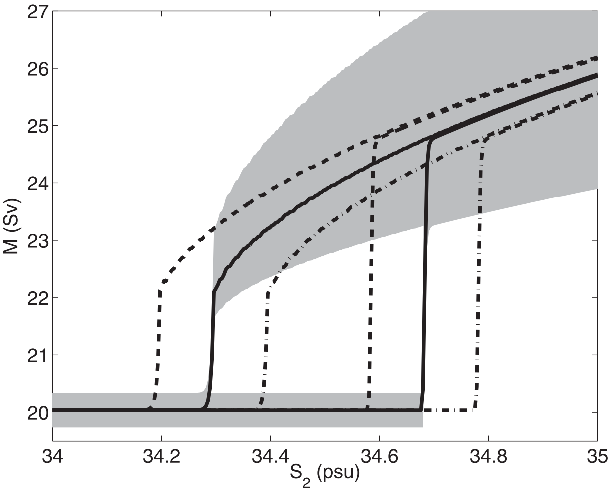

FIG. 4. Volume transport M as a function of S_2, range of daily data (gray), and annual averages (black solid) for $S_4 = 34.9$ psu. Annual-average data are also shown for experiments with $S_4 = 34.8$ (dashed) and 35 psu (dashed–dotted).

The salinity of the upper boundary current is just one of the factors controlling the salinity of the upper central basin, the other being surface freshwater flux [Eq. (2)]. For the standard salinity $S_2 = 35$ psu, all realistic values of freshwater flux yield a strong circulation mode (not shown). However, for a salinity within the hysteresis, $S_2 = 34.5$ psu, a wide range of surface freshwater fluxes supports two stable modes of circulation (Fig. 5).

As a consequence of hysteresis, short variations in boundary conditions such as pulses of surface freshwater flux and boundary current salinity potentially yield persistent changes in the SPG circulation. A reduction in surface freshwater flux from 1 to 0.5 m yr^{-1} ($S_2 = 34.5$ psu) during 4 yr is sufficient to cause a strengthening of the SPG and is used here to illustrate the chain of events that lead to the intensification (Fig. 6). The model is initialized without baroclinic circulation and reaches the equilibrium of temperature and salinity in both the upper and lower basin after a few years. Between years 10 and 13, surface freshwater flux is reduced to 0.5 m yr^{-1}, which allows the surface salinity to rise and to initiate deep convection. Mixing with the deep water mass increases the surface salinity sharply while the lower basin cools in convective contact with the cold surface. Thus, the baroclinic transport in upper and lower levels increases and eddy salt transport into the upper central basin also increases. The now constantly higher surface salinity allows for convection in every cold season and a sustained baroclinic circulation, even after the surface freshwater flux perturbation is switched off.

After the spinup of the SPG, the average velocity of the lower boundary U_2 increases by 0.024 m s^{-1} (Fig. 7). The velocity of the upper boundary current U_1 increases on average by 0.037 m s^{-1}, where more than half is due to the higher U_2 that also adds to U_1 [Eq. (11)]. Notably, U_1 shows large intra-annual variability as a result of the seasonal temperature changes. During summer, temperatures in the upper central basin are high enough to

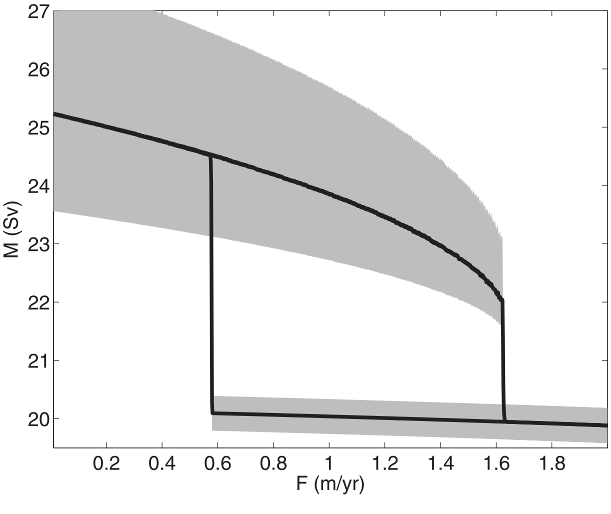

FIG. 5. Volume transport M as a function of F (at $S_2 = 34.5$ psu), range of daily data (gray), and annual averages (black).

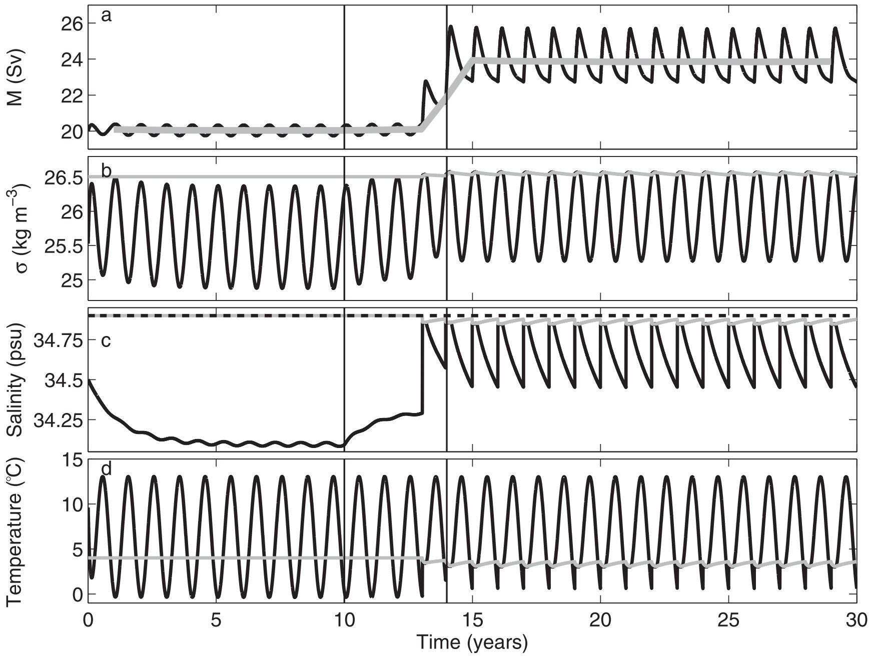

FIG. 6. As in Fig. 2, but for $S_2 = 34.5$ psu, showing the response to a 4-yr reduction of F from 1 to 0.5 m yr^{-1} (vertical lines).

induce an anticyclonic flow that works against the cyclonic barotropic flow, thus weakening the SPG. Seasonal variations, albeit of smaller amplitude, are also observed in U_2. The sharp increase in lower boundary current velocity during winter is due to the convective cooling of the lower central basin. The simultaneous freshening is negligible. Because the vertical extent of the lower boundary current is 14 times that of the upper boundary current, its volume transport increases by 3.42 Sv compared to the 0.37 Sv increase of the upper boundary current.

Other perturbations of the surface freshwater balance have similar consequences. However, remote freshwater perturbations are not only advected to the Labrador Sea by surface currents. Surface freshening in the Nordic seas and the Arctic Ocean may decrease the density of the deep overflows across the Greenland–Scotland Ridge, with a direct impact on Icelandic Slope Water (i.e., S_4). A 1-yr decrease in the salinity of the lower boundary current by 0.2 psu increases the density contrast in the lower level (Fig. 8). This has two consequences that eventually lead to a permanent spinup of the SPG. First, the faster circulation intensifies eddy mixing at the surface and the salt flux into the upper central basin, thus lowering the convection threshold. Second, the decreased salinity in the lower boundary current causes the density of the lower central basin to decrease, again facilitating deep convection. In summary, the short-lived reduction in salinity is sufficient to establish the regime with regular deep convection and therefore a strong SPG circulation.

c. Sensitivity to the wind-driven transport and the depth of convection

We now turn to changes in remote forcing that are not explicitly simulated by the simplified model and may have a strong impact on the SPG and its two stable modes of circulation. The strength of the depth-invariant

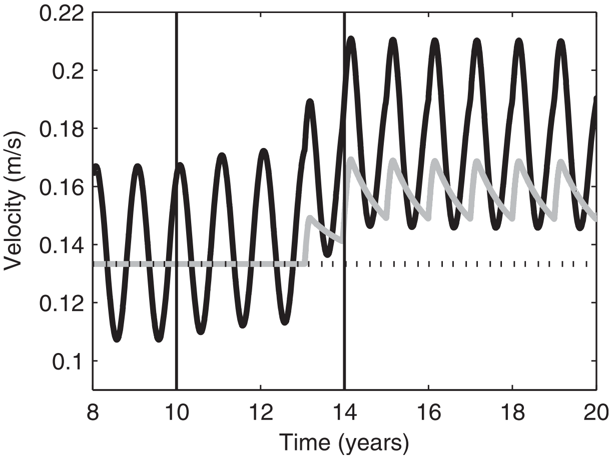

FIG. 7. Velocities of upper (U_1, black) and lower (U_2, gray) boundary current and the barotropic velocity (dotted) for the experiment with reduced surface freshwater flux between years 10 and 14 (see Fig. 6).

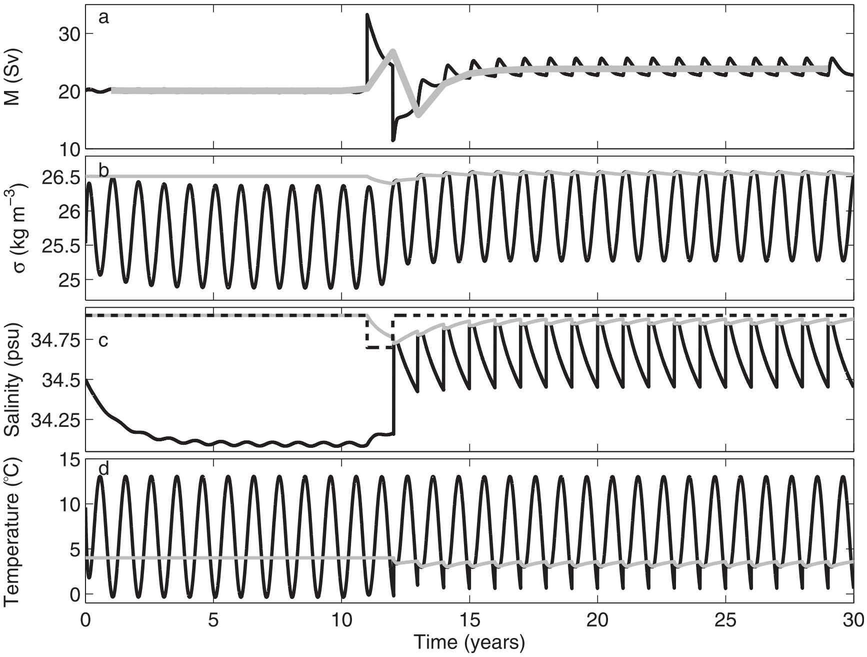

FIG. 8. As in Fig. 2, but for $S_2 = 34.5$ psu, showing the response to a 1-yr decrease of S_4 by 0.2 psu in year 11.

transport M_{btp} is incremented from 1 to 100 Sv in steps of 1 Sv. The weak and strong circulation modes are chosen explicitly by setting the salinity of the upper boundary current to $S_2 = 34$ and 35 psu, respectively, for which only monostable solutions exist (Fig. 4). For each increment, the model is run into equilibrium for 30 yr. Two stable modes of circulation exist for the entire range of M_{btp} with the exception of the weak circulation below $M_{\mathrm{btp}} = 10$ Sv that does not produce a stable result (Fig. 9). The weak circulation mode remains largely unchanged with stronger barotropic forcing, which is expected because a baroclinic circulation cannot exist under the chosen boundary conditions. Maybe surprisingly, the strong circulation mode becomes weaker as the barotropic circulation increases, not only relative to the increasing barotropic circulation but also in absolute terms. This is because a stronger baseline circulation does not only enhance eddy salt flux into the upper central basin, increasing the radial density difference, but it also removes density anomalies from the lower basin more efficiently. Additional salt advection by the baroclinic circulation and the positive advection–convection feedback become less relevant with higher barotropic transports. This is equivalent to reducing the height of the hysteresis in Figs. 4 and 5 as well as their width. Comparing the respective contributions of the barotropic and baroclinic circulation components to the total, we find that they are approximately equal for a barotropic transport of 8 Sv. For barotropic transports above 38 Sv the baroclinic part contributes less than 10% to the total and less than 5% above 54 Sv.

The barotropic contribution to the total SPG transport is uncertain, and it is probably represented very differently in general circulation models. Similarly, the depth of convection is different in different models and has shown variability in observations over recent decades (Yashayaev 2007). Different depths of convection are analyzed by changing the depth of the lower boxes d from 0, representing a Labrador Sea in which the upper ocean does not communicate with deeper layers at all, to 3000 m, the full depth of the basin. As for M_{btp}, all other model parameters are kept at their default values and the model is run into equilibrium for 30 yr. The baroclinic transport, when active, increases approximately linearly with the depth of convection (Fig. 10).

4. Analytical solution

The analysis of the four-box model shows that the following chain of events leads to an enhanced SPG circulation. When the surface density of the central basin exceeds that of the underlying water mass and convection sets in, atmospheric cooling increases the density of the entire water column. The enhanced radial density gradient strengthens the thermal wind in the boundary current. Consequently, eddy salt flux increases from the saline upper boundary current into the relatively fresh upper central basin. This flux of salt increases the surface

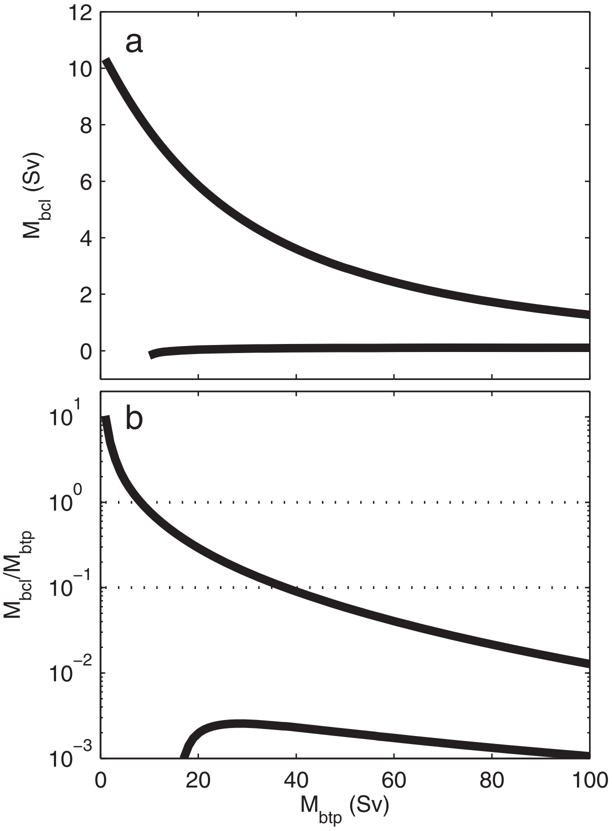

FIG. 9. (a) Absolute and (b) relative strength of baroclinic transport component M_{bcl} as a function of M_{btp}. The contribution of barotropic and baroclinic parts to the total circulation is approximately equal for a barotropic transport of 8 Sv. For barotropic transports above 38 Sv, the baroclinic part contributes less than 10% of the total.

density that in turn lowers the convection threshold, closing a positive feedback loop.

Although the spinup of the SPG is mainly due to the lower boundary current, it has direct consequences for the eddy salt flux at the surface. Moreover, the upper boundary current velocity contributes only marginally to the changes so that the boundary current dynamics can adequately be simplified into a single layer. Similarly for the central basin, convection is essential for the intensification of the SPG circulation, and the convective mixing also effectively reduces the two layers into one. Note that convective events are aided but not directly caused by the enhanced salt flux but by the prescribed low winter temperatures. Therefore, the reduction to a single central basin can be considered the result of external parameters of the four-box model and as such can equally be well imposed by choosing a single central basin from the outset.

Based on this understanding, the four-box model can be simplified to two boxes, one for the central basin and one for the boundary current. As before, temperature

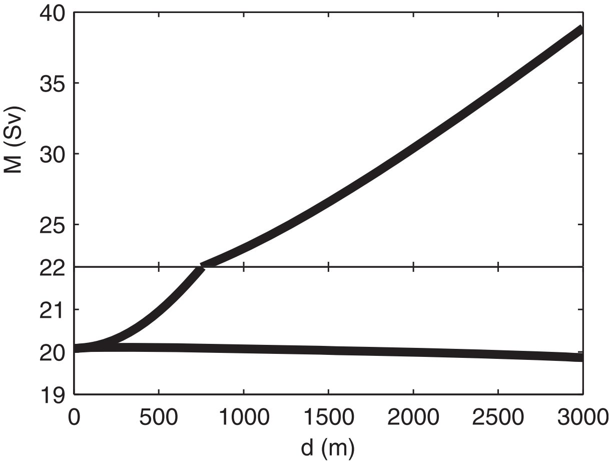

FIG. 10. Bifurcation diagram for depth of lower boxes d.

and salinity of the boundary current (T_2, S_2) are prescribed. In addition, without the shallow surface layer that quickly adjusts to atmospheric temperatures, the temperature of the central basin (T_1) is fixed here as well. These assumptions lead to one equation describing the freshwater balance of the central basin and a second equation for the dynamics of the cyclonic circulation:

$$Ac^{*}U_{\mathrm{bcl}}(S_1 - S_2) = -S_0A'F \quad \text{and} \tag{17}$$

$$U_{\mathrm{bcl}} = k\Delta\rho = k[\beta(S_1 - S_2) - \alpha(T_1 - T_2)], \tag{18}$$

where constants c^{*}, S_0, α, and β are the same as before, $k = -gh(f\rho_0 w)^{-1}$ is the baroclinic flow efficiency, A' is the surface area of the central basin, and A is the interface between the center and boundary current. The term U_{bcl} is the baroclinic velocity of the boundary current. The barotropic part is not considered here. The values T and S are temperatures and salinities of the central basin (subscript 1) and boundary current (subscript 2). Combining Eqs. (17) and (18) yields the quadratic equation

$$U_{\mathrm{bcl}}^2 + k\alpha(T_1 - T_2)U_{\mathrm{bcl}} + \frac{k\beta}{c^{*}}\frac{A'}{A}S_0F = 0, \tag{19}$$

with the two solutions

$$U_{\mathrm{bcl},\pm} = -\frac{1}{2}k\alpha(T_1 - T_2) \pm \sqrt{\frac{1}{4}k^2\alpha^2(T_1 - T_2)^2 - \frac{k\beta}{c^{*}}\frac{A'}{A}S_0F}. \tag{20}$$

This solution is formally similar to the solution of Stommel's model of AMOC and subsequent interpretations (Stommel 1961; Marotzke 1990; Rahmstorf 1996;

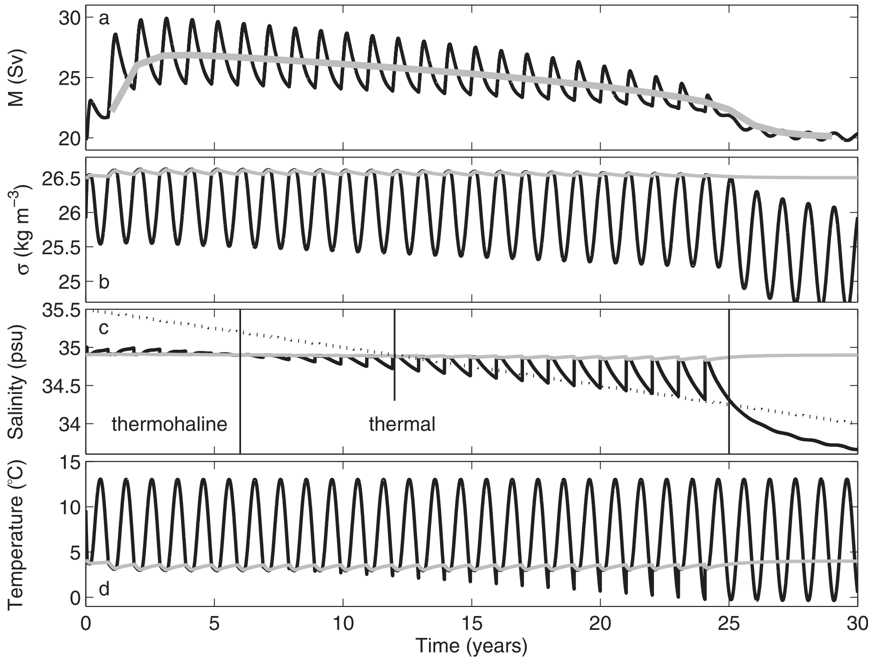

FIG. 11. As in Fig. 2, but for externally forced, linearly decreasing salinity in the upper boundary current S_2 [dotted in (c)]. In the convective basin, salinity is higher at the surface for high S_2 and consequently transported downward during convection events. Both salinity and temperature contribute to increasing the density of the lower basin. This changes with lower S_2, when convection is caused by cooling exclusively, despite a freshwater barrier.

Marotzke 2000). Similar dynamics have also been found for convection in a marginal sea (Spall 2012), although this model describes two modes for the temperature difference $T_1 - T_2$ instead of U_{bcl}. As discussed in these previous works, only the solution with the positive sign produces a stable circulation. The two solutions meet in a saddle-node bifurcation when the square root becomes zero.

The analytical model adds significant understanding to the more complex four-box model. The nonlinearity of the SPG circulation is not an artifact of deep convection that itself is a highly nonlinear process. Unlike in the four-box model, convective mixing is not explicitly included in the analytical model. Instead, nonlinearity and bifurcation are results of the quadratic term in Eq. (19) that stems from the feedback of salt transport and the intensity of the circulation, similar to Stommel's salt advection feedback.

a. Flow regimes

The formal similarity of the analytical solution to previous models of the AMOC allows us to adopt their characterization of different flow regimes based on values for T_1, T_2, and F in Eq. (20). For $T_1 < T_2$ and $F < 0$, both temperature and salinity drive the SPG circulation, thus referred to as the thermohaline mode. For $T_1 > T_2$ and $F < 0$, the surface freshwater flux drives the circulation while temperature counteracts the haline mode and vice versa for the thermal mode with $T_1 < T_2$ and $F > 0$.

Although these modes strictly apply only to the analytical model with reference to the temperature difference between the center and boundary current, analogs can be found in the more complex four-box model that passes from the thermohaline to the thermal circulation mode as S_2 decreases (Fig. 11). Eddy salt transport from the upper boundary current into the upper central basin effectively counteracts surface freshwater flux at the beginning of the experiment until approximately year 6, so that the salinity of the upper central basin S_1 is higher than for the underlying water mass S_3. Therefore, both salinity and temperature help drive deep convection and increase the density of the lower central basin over that of the lower boundary current, driving the circulation in the thermohaline regime. From year 12 until the shutdown of the baroclinic circulation in year 24, surface freshwater flux is absorbed only partly in the upper boundary current while an increasing amount is mixed into the lower central basin and from there into the lower boundary current. The density of the lower central basin is still higher than in the lower boundary current, keeping the baroclinic circulation active, but only because of the cooling from above while salinity counteracts. This is the thermal regime. In the four-box model, the thermal regime can be further divided into two parts, characterized by freshwater fluxes. After year 12, the upper boundary current becomes less saline than the lower (34.9 psu) and turns into an additional source of freshwater, while convection is still active. The flows of heat and freshwater between sources and sinks are summarized for both models in Fig. 12, illustrating the similarities of heat and freshwater fluxes for thermohaline and thermal regimes. The haline regime, for which the temperature of the central basin must be higher than that of the boundary current, is deemed unrealistic in the present context.

With its parameters at their default values ($S_2 = 35$ psu), the four-box model operates in the thermal flow regime. The salinity of the lower central basin is below that of the lower boundary current (Fig. 2). This is consistent with observations that find Labrador seawater colder but fresher than the boundary current. Note that the thermal regime is relatively close to the shutdown of the baroclinic circulation.

b. *Critical freshwater flux*

The bifurcation point of the analytical model defines a critical freshwater flux F_{crit} that is the upper limit for a baroclinic circulation to exist. The two solutions of Eq. (20) combine in a bifurcation when the term of the square root vanishes, so that

$$F_{\mathrm{crit}} = \frac{k\alpha^2 c^*}{4\beta S_0}\frac{A}{A'}(T_1 - T_2)^2 \quad \text{and} \tag{21}$$

$$U_{\mathrm{bcl}}^{\mathrm{crit}} = -\frac{1}{2}k\alpha(T_1 - T_2). \tag{22}$$

The critical surface freshwater flux increases quadratically with rising temperatures as the difference between the central basin and boundary current. However, for the temperature difference found in the four-box model (0.83°C), the critical freshwater flux is only 0.91 m yr^{-1} or 8.16 mSv. This is considerably lower than in the four-box model (Fig. 5) and implies that perturbations like the Great Salinity Anomaly (GSA) with approximately 6.5 mSv on top of the climatological average (Curry and Mauritzen 2005) could have pushed the SPG past the bifurcation point. Thus, the circulation in the more complex model, and probably in the real-world SPG, is more robust than in the analytical model. It also illustrates the limited usefulness of the analytical model for quantitative purposes. Qualitatively, however, we conclude that a larger temperature difference increases the width of the hysteresis.

5. Discussion

a. *Freshwater flux and bistability*

The loss of buoyancy at the surface drives a sizable part of the circulation (10%–25%). Winter cooling and deep convection increase the density of the water column and produce a dense water core around which lighter waters circulate cyclonically. This baroclinic flow adds to the externally driven barotropic flow, strengthening the eddy salt transport into the upper central basin and lowering the convective threshold. Thus, when the baroclinic circulation is active, it partly contributes to sustain itself. If it is not active, eddy salt flux into the central basin might be too low to offset surface freshwater flux. In this case, convection does not occur and the baroclinic part of the circulation does not start. The SPG remains in a barotropic, weak mode of circulation. As a consequence, two stable equilibria exist for upper boundary current salinities between 34.34 and 34.7 psu, depending on the initialization of the model and its history. A hysteresis is found for parameters that modify the eddy salt flux in the upper layer, namely the salinity of the boundary current and surface freshwater flux into the central basin.

Considerable evidence suggests that this idealized model qualitatively describes the bistability found in several general circulation models (Levermann and Born 2007; Born et al. 2009; Born and Mignot 2012; Born et al. 2012). As one example from a current coupled model, Fig. 13 shows composites of the March mixed layer depth and the depth-integrated streamfunction of the Community Climate System Model, version 4 (Gent et al. 2011). During the second half of a 1000-yr-long present-day control integration of this model, the SPG spontaneously switches into a strong circulation mode and then back again after almost 150 yr [for details see Born et al. (2012)]. To objectively distinguish these two modes, we define composites that exceed plus or minus one standard deviation of the streamfunction averaged over the western part of the basin. The strong circulation is associated with deep convection in the Labrador Sea where the cyclonic flow increases by approximately 7 Sv. This increase, albeit weaker, is observed throughout the western basin and the southern part of the SPG. With a weaker circulation, deep convection in the Labrador Sea is missing, while some compensation is seen in the Irminger Basin and the Iceland Sea. However, this does not notably strengthen the cyclonic flow there. One important conclusion from the analysis of the complex model is that the SPG is indeed within the bistable range of parameters and close to a critical threshold in present-day climate, as suggested by the thermal flow regime found in the analytical solution of our model.

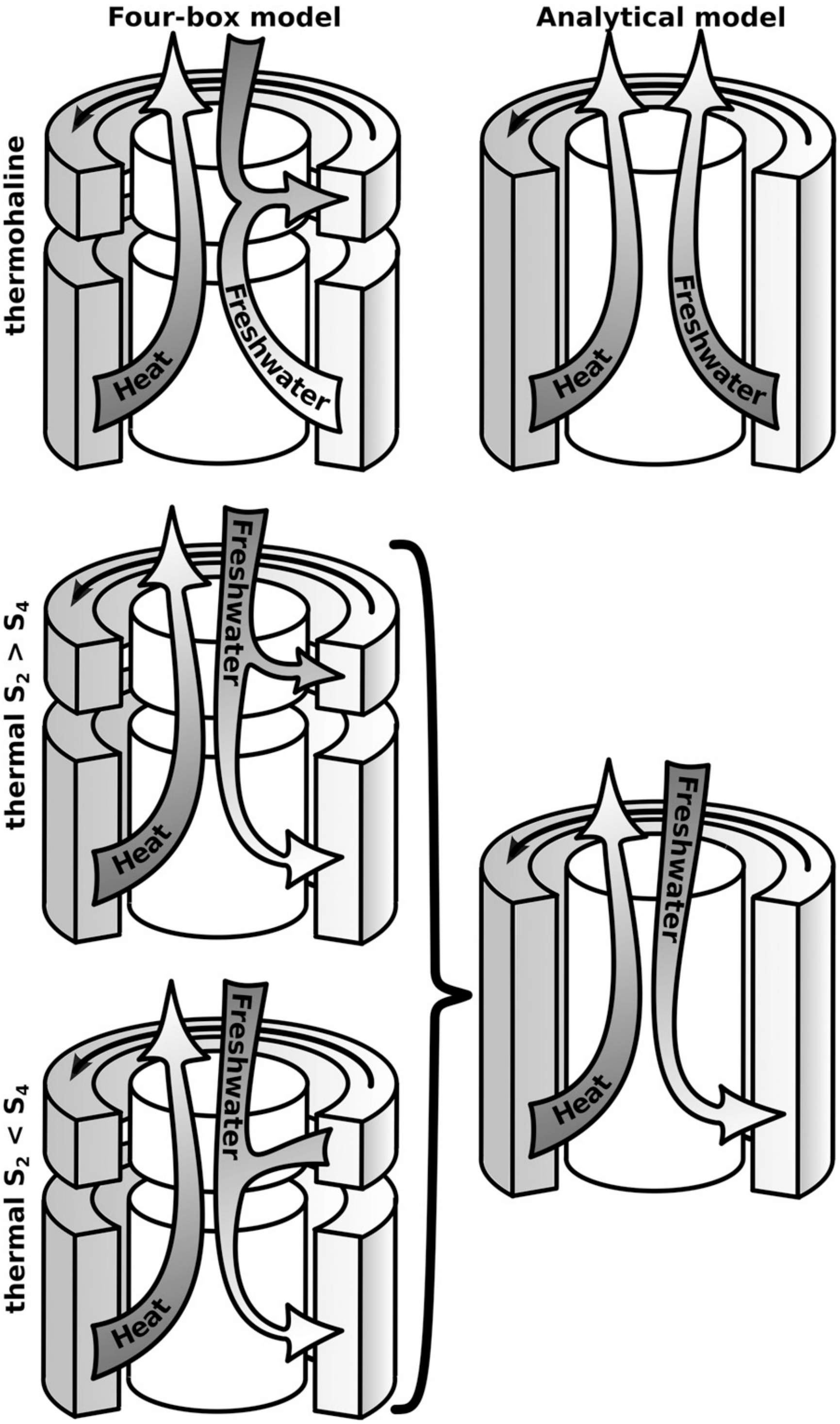
Four-box model
Analytical model
thermohaline
thermal $S_2 > S_4$
thermal $S_2 < S_4$
Heat
Freshwater

FIG. 12. Schematic of heat and freshwater flows between sources and sinks in the four-box and analytical model, for the thermohaline and thermal regime. The thermal regime is split in two in the four-box model, depending on the salinity of the upper boundary current. Despite the differences in model formulation, flows of freshwater and heat qualitatively agree in both models.

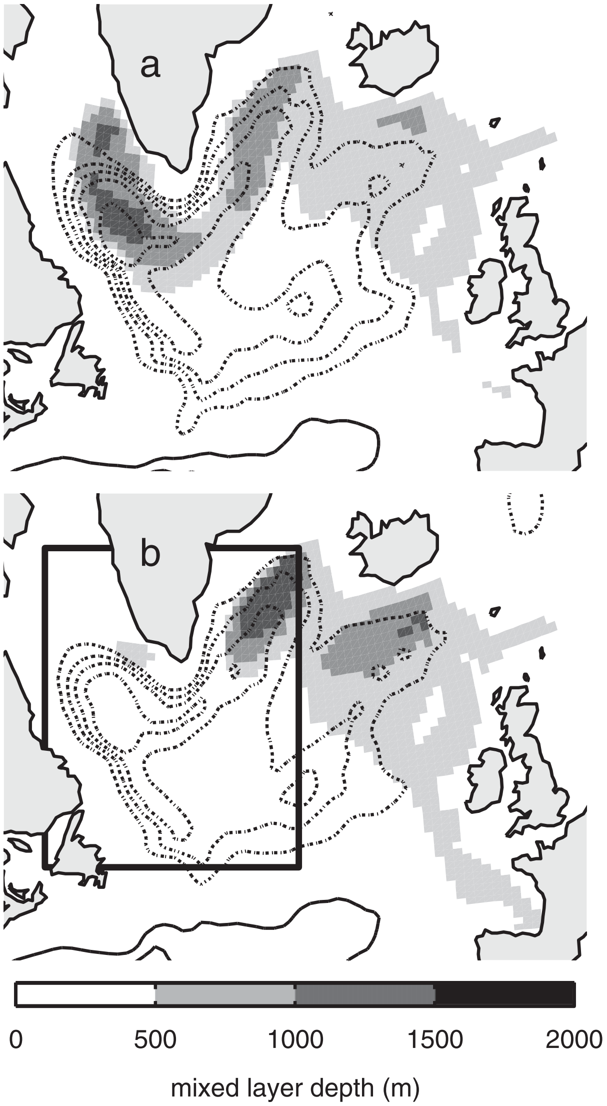

FIG. 13. Composite mixed layer depth (shading) and depth-integrated streamfunction (contours, spacing 10 Sv, negative dashed, zero omitted) in the Community Climate System Model, version 4, for (a) strong SPG (max transport 55.8 Sv) and (b) weak SPG (max transport 46.4 Sv). The strength of the circulation is defined as the average of the streamfunction in the western basin (black rectangle).

Transitions from the weak to the strong mode of circulation are triggered by an intermittent increase in the salinity of the upper boundary current or a reduction in the surface freshwater flux. Both act to increase eddy salt flux into the upper central basin temporarily and to initiate convective cooling of the underlying water mass. The subsequent intensification of the boundary current increases eddy salt flux permanently. Interestingly, a freshwater pulse in the lower boundary current also causes a transition to the strong mode of circulation. It causes a short-lived increase in the density gradient between the lower central basin and the boundary current, increasing the eddy salt flux into the upper central basin. At the same time, the lower salinity in the lower boundary current increases salt export from the lower central basin, decreasing its density. Both these changes favor convection that, once it sets in, permanently establishes a stronger circulation. A similar behavior has been observed in a low-resolution ocean general circulation model (Levermann and Born 2007). This result has important implications for the sensitivity of the SPG to freshwater forcing, in particular from Arctic sources. A freshwater pulse that reaches the convection regions of the Nordic seas will impact the density of the Greenland–Scotland Ridge overflows and tends to strengthen the SPG circulation. However, if the perturbation of freshwater is not transported into the deep ocean but reaches the SPG at the surface, the effect is the opposite.

The inclusion of both temperature and salinity is critical for the bistability. For the nonlinearity to exist, the central region must both be denser than the boundary current to drive a baroclinic flow and at the same time allow an exchange with the boundary current that increases the density of the interior region. This cannot be reconciled with a single temperature or density variable. Models that make this simplification, as is common in the case of the SPG (Spall 2004; Straneo 2006b; Deshayes et al. 2009), neglect a crucial feedback mechanism and are therefore not expected to be bistable.

b. *Wind-driven circulation*

Our flat-bottomed model does not include vorticity input by baroclinicity that adds to the barotropic flow component through the joint effect of baroclinicity and relief (JEBAR; Mellor et al. 1982; Mertz and Wright 1992). This complicates the decomposition into buoyancy and wind-driven forcing because the former could add to the depth-invariant circulation that here is represented as the external model parameter M_{btp}. However, the effect of stronger winds can be tested qualitatively. As they become stronger and the barotropic circulation more intense, the baroclinic circulation weakens. This is attributed to the more efficient removal of high-density waters from the lower central basin, equivalent to the export of Labrador seawater, thus reducing the density difference between the center and boundary current. Barotropic and baroclinic components contribute equally to the total SPG transport of the latter, an external parameter in our model that is chosen at 8 Sv. For a more realistic transport of 20 Sv, the baroclinic part contributes about 23% and less than 10% for external forcings that drive more than 38 Sv of barotropic flow. However, the idealized model does not include the effect of enhanced salt advection by a stronger circulation. A stronger wind-driven flow would also transport more salt from the relatively saline eastern subpolar North Atlantic to the western part of the basin and increasingly offset Arctic freshwater export in the East Greenland Current (Born et al. 2013). Thus, the salt transport feedback is probably stronger than considered here when the advective component is taken into account. We speculate that this would offset some of the weakening of the baroclinic circulation caused by stronger winds in the simplified model or even lead to an increase, as suggested by the analysis of SPG variations over the last millennium (Moffa-Sánchez et al. 2013, manuscript submitted to *Nat. Geosci.*).

An important caveat related to the relative strengths of barotropic and baroclinic transports stems from the representation of eddy fluxes in our model. For simplicity but without a strong theoretical basis, we assume the same efficiency for eddies resulting from both barotropic and baroclinic instabilities. Different efficiencies may change the relative importance of wind- and buoyancy-driven transports.

The superposition of wind- and buoyancy-driven circulation is one major difference between our model and the similar approach by Straneo (2006b), where the vertical average of velocity is assumed to be constant. This earlier study finds that an increase in the externally forced circulation weakens the sinking of water masses and therefore overturning. Although the model presented here does not explicitly address sinking, a water mass transformation takes place in density space. A stronger externally forced circulation in our model results in a stronger eddy exchange at the surface, thus a salinification of the central upper basin, which makes deep convection more efficient. The also enhanced eddy flux in the lower layer then acts to export the convection product more efficiently from the basin. Therefore, qualitatively, a stronger circulation entails a stronger overturning in our model. The strength of the wind-driven part of the SPG is virtually unknown in both observations and models. However, the simulated strength of the SPG in models covers a wide range (Born et al. 2012), which is likely reflected in the wind-driven part of the circulation. Because the importance of the buoyancy-driven part of the circulation decreases with stronger winds and the separation of the strong and weak mode of circulation, the present work suggests that models with a relatively strong SPG are less prone to large amplitude changes in the SPG. Note that the strength of the SPG circulation also scales with horizontal model resolution (Treguier et al. 2005; Born et al. 2012).

Our model bears similarities with the two-box models of deep convection by Welander (1982), Rahmstorf (2001), and Kuhlbrodt et al. (2001). The primary difference is the inclusion of the boundary currents and their impact on heat and salt fluxes to the convective center, where previous studies employed a restoring condition. In a recent description of deep convection, Spall (2012) discusses a model with similar characteristics as our analytical solution, including eddy fluxes of heat and salt proportional to the baroclinic shear velocity. Their critical value for precipitation that shuts down deep convection is the same as our Eq. (21). This last study also identifies two modes of circulation. However, while one mode is thermally driven and related to active deep convection, thus similar to the strong baroclinic mode in our model, the second mode is characterized by a reverse circulation driven by salt exclusively. This is analogous to the haline mode in Stommel's model. In contrast, we describe two stable modes of cyclonic circulation.

Earlier work on the sensitivity of the SPG to changes in wind stress with an ocean general circulation model emphasized the importance of the Greenland–Scotland Ridge overflow transport (Montoya et al. 2011), which is not included in our idealized model. In the absence of overflows, specifically with boundary conditions for the Last Glacial Maximum, the SPG strength increases with stronger winds in agreement with our model. However, for present-day boundary conditions with an active overflow, the strength of the SPG decreases with stronger winds because of increasing overflows that modify the water mass equivalent to the lower boundary current in the four-box model. While we cannot rule out this possibility, it appears to contradict studies that find a positive correlation of the gyre circulation with winds over the eastern subpolar North Atlantic (Häkkinen et al. 2011; Langehaug et al. 2012), albeit with much smaller variations in wind stress than those of Montoya et al. (2011). It is important to acknowledge the imperfect representation of overflow transport in the mentioned ocean model due to its coarse resolution (Montoya et al. 2005; Born et al. 2009). On the other hand, high-resolution models corroborate a considerable increase in overflow transport with stronger winds (Biastoch et al. 2003) and a strong impact on the circulation of the SPG (Böning et al. 1996). Changes in the density of the lower boundary current typical of variations in overflow transport have a large effect in our model (Fig. 8). Clearly, future simulations are needed to resolve remaining questions regarding the effects of overflows and wind stress on the SPG.

The conceptual distinction between wind- and buoyancy-driven circulation proposed here, and their regionalization to the eastern and western basin, respectively, may contribute to the understanding of how atmospheric patterns of variability impact the SPG. Variations in the North Atlantic Oscillation (NAO) that have been found to correlate well with the SPG (Curry and McCartney 2001; Böning et al. 2006) might be more important for buoyancy fluxes in the western part of the basin, thus driving variations in the SPG mainly through its buoyancy-driven part. In contrast, changes in the EAP drive the SPG primarily through the wind-driven circulation in the eastern part of the basin (Häkkinen et al. 2011; Langehaug et al. 2012). The idealized model provides a testable hypothesis of how these two modes of variability interact on the SPG and might help to clarify the attribution of observed variability.

c. Shortcomings of the simplified model

Several simplifying assumptions were made for the formulation of the four-box model, some of which might affect one of the major findings of this study, the bistability. First, the depth of convection is considered constant. In reality, warm winters do not necessarily shut down convection completely but allow for some mixing to a shallower depth (Yashayaev 2007). This probably permits additional stable equilibria for the strong circulation mode, possibly even a continuous spectrum. As a second caveat, we neglect variations in atmospheric temperatures over the Labrador Sea that are known to vary considerably. In its present form, the model initiates deep convection as soon as the oceanic prerequisites are met, assuming atmospheric temperatures favorable of convection recur every winter. This is not the case in the present-day climate. These shortcomings, combined with the already discussed uncertainties regarding the Greenland–Scotland Ridge overflow transport, may result in a hysteresis that is smaller and more difficult to find in more complex models as well as the real world. Temperatures and salinities of the boundary currents are constant in our model, thus neglecting heat and salt loss to the central region. This simplification is not realistic for the Labrador Sea (Spall 2011, 2012). Its effect is that more heat and salt are transported into the convective center than with more realistic, interactive tracer concentrations. However, other model parameters and related uncertainties likely have a stronger impact, for example, the eddy flux efficiency or the circumference of the central basin. For the boundary current itself, a decreasing density along its path results in a weaker thermal wind and consequently a vertical downwelling velocity to ensure continuity (Straneo 2006b). Neither this nor the implications for heat and salt budgets are considered in the present model.

However, we argue that this does not lessen the importance of the positive feedback mechanism involving the transport of salt into the western subpolar North Atlantic and the associated amplification of variability, which indeed have been found in many more complex models (Levermann and Born 2007; Born et al. 2010b; Born and Mignot 2012; Mengel et al. 2012; Born et al. 2012, 2013). Observations of the second half of the last century find a 17 Sv difference in the flow of the North Atlantic Current between 1970 and the early 1990s, approximately 30% of the time-average transport, of which one-half is attributed to the SPG (Curry and McCartney 2001). The same study ascribes this change mainly to buoyancy forcing and thus the baroclinic circulation. The magnitude of change and assumed mechanism are in good agreement with the baroclinic circulation in our model, suggesting that the nonlinear threshold might have been passed during that time. Strong support for this conclusion comes from recent work describing a hysteresis behavior of the AMOC with respect to Arctic freshwater export (Dima and Lohmann 2011). They identify the SPG as the key center of action and find several rapid transitions during the past 150 yr.

6. Summary and outlook

We present a conceptual, four-box model of the western Atlantic subpolar gyre and the Labrador and Irminger Seas. It consists of a cylindrical interior region encircled by a boundary current. Both regions are vertically divided into an upper layer of 100-m thickness and a lower layer that reaches a depth of 1500 m. The two layers of the boundary current are in contact only with their respective counterpart of the central basin through parameterized eddy fluxes of heat and salt. In the central basin, upper and lower water masses are mixed by convection when the stratification becomes unstable. The model is forced by a seasonal cycle of temperature and a fixed freshwater flux in the central region. The wind-driven circulation, temperature, and salinity of the boundary current are external parameters and are tested for their impact on the SPG circulation.

The main conclusions are summarized in three points:

- The buoyancy-driven part of the SPG contributes up to one quarter of the total flow, but its importance for variability is probably larger due to its nonlinear dynamics.
- Two stable modes of circulation are found in the simplified model, which resembles circulation anomalies in more complex models. A hysteresis is found for surface freshwater flux and the remotely advected salinity of the boundary current.
- The bistability is not a direct consequence of the nonlinearity of the convective process. Rather, it is caused by the mutual strengthening of the boundary current and associated salt transport.

The term advective–convective feedback has previously been used to describe the dynamics of the subpolar gyre in coupled climate models (Born et al. 2012). The present model specifies that the bistability is indeed a combination of the convective feedback of Welander (1982) and the advective (here eddy turbulent) feedback first described by Stommel (1961). While the present study focuses on the western subpolar North Atlantic, the model is in general applicable to other recirculation systems around a convective core. Therefore, hypothetically, the Nordic seas, the Weddell Sea, or the Gulf of Lion exhibit similar dynamics.

a. Past changes in the SPG

This improved understanding of the SPG dynamics provides a basis for studies of climate variability over a broad range of time scales. In agreement with the mechanism presented here, it has been suggested that the freshwater pulse of the so-called 8.2-ka event caused a transition from a weak to strong SPG that eventually led to the onset of Labrador Sea convection approximately 8200 yr before present (Born and Levermann 2010). It is conceivable, however, that this transition was not a singular event during the present interglaciation, but rather a modulation of relatively frequent transitions, as have been documented for the entire Holocene (Thornalley et al. 2009; Colin et al. 2010; Montero-Serrano et al. 2011) and in more detail for the last millennium (Moffa-Sánchez et al. 2013, manuscript submitted to *Nat. Geosci.*). In the context of our simplified model, the difference of these two interpretations relates to the width of the hysteresis and therefore the stability of the two individual modes of circulation.

Frequent transitions of the SPG indicate that the system is near its critical threshold in the present climate. This was probably different in the previous interglaciation, the Eemian, when a different configuration of the Earth's orbit caused the Arctic to receive more solar irradiation during summer. Consequently, less sea ice was exported to the North Atlantic, leading to denser surface waters and a stabilization of the strong SPG mode (Born et al. 2010b; Irvali et al. 2012). The increase of Arctic sea ice export during the subsequent glacial inception was simulated to cause an intermittent weakening of the SPG and a temperature fingerprint that has been reconstructed from climate proxy archives (Born et al. 2010a, 2011).

b. Recent changes and future evolution

Recent decades have seen large shifts in the SPG circulation (Häkkinen and Rhines 2004; Hátún et al. 2005; Lohmann et al. 2009a) and, associated with that, in the heat content of the subpolar North Atlantic (Robson et al. 2012; Yeager et al. 2012). Despite several attempts to link the dynamic changes to atmospheric and oceanic forcing (Lohmann et al. 2009b; Häkkinen et al. 2011) and to decompose driving factors statistically (Langehaug et al. 2012), results must still be considered preliminary. The present study contributes to this discussion with a decomposition based on first principles, providing guidance for future changes that, because of the inherent nonlinearity of the SPG, might not be accurately projected from recent variations.

Climate projections of the twenty-first century find an increase in Arctic freshwater export through Fram Strait of 61–146 mSv (Holland et al. 2006; Swingedouw et al. 2007; Lehner et al. 2012) that would be enough to transition the SPG into the weak circulation mode. The consequential reduction in salt flux would aid a shutdown of Labrador Sea deep convection, with probably large consequences for the Atlantic meridional overturning circulation and the associated interhemispheric heat transport (Vellinga and Wood 2002; Latif et al. 2006).

Progress in the topical field of decadal climate predictability is severely hampered by shortcomings in the understanding of crucial mechanisms. Although skillful predictions are theoretically feasible for up to 20 yr into the future (Msadek et al. 2010), current prediction systems achieve much less. The SPG being one of the regions with the highest predictive skill (Matei et al. 2012), future development and applications of the concept presented here might help to advance this important area of research.

Acknowledgments. A. B. received financial support from the European Commission under the Marie Curie Intra-European Fellowship ECLIPS (PIEF-GA-2011-300544) and the National Centre for Excellence in Research: Climate of the Swiss National Science Foundation. We are grateful for comments from two anonymous referees and Editor Michael Spall.

REFERENCES

Biastoch, A., R. H. Käse, and D. B. Stammer, 2003: The sensitivity of the Greenland–Scotland Ridge overflow to forcing changes. *J. Phys. Oceanogr.,* **33,** 2307–2319.

Böning, C. W., and F. Bryan, 1996: Large-scale transport processes in high-resolution circulation models. *The Warmwatersphere of the North Atlantic Ocean,* W. Krauss, Ed., Gebrüder Borntraeger, 91–128.

——, ——, W. R. Holland, and R. Döscher, 1996: Deep-water formation and meridional overturning in a high-resolution model of the North Atlantic. *J. Phys. Oceanogr.,* **26,** 1142–1164.

——, M. Scheinert, J. Dengg, A. Biastoch, and A. Funk, 2006: Decadal variability of subpolar gyre transport and its reverberation in the North Atlantic overturning. *Geophys. Res. Lett.,* **33,** L21S01, doi:10.1029/2006GL026906.

Born, A., and A. Levermann, 2010: The 8.2 ka event: Abrupt transition of the subpolar gyre toward a modern North Atlantic circulation. *Geochem. Geophys. Geosyst.,* **11,** Q06011, doi:10.1029/2009GC003024.

——, and J. Mignot, 2012: Dynamics of decadal variability in the Atlantic subpolar gyre: A stochastically forced oscillator. *Climate Dyn.,* **39,** 461–474, doi:10.1007/s00382-011-1180-4.

——, A. Levermann, and J. Mignot, 2009: Sensitivity of the Atlantic Ocean circulation to a hydraulic overflow parameterisation in a coarse resolution model: Response of the subpolar gyre. *Ocean Modell.,* **27** (3–4), 130–142.

——, M. Kageyama, and K. H. Nisancioglu, 2010a: Warm Nordic seas delayed glacial inception in Scandinavia. *Climate Past,* **6,** 817–826, doi:10.5194/cp-6-817-2010.

——, K. H. Nisancioglu, and P. Braconnot, 2010b: Sea ice induced changes in ocean circulation during the Eemian. *Climate Dyn.,* **35,** 1361–1371, doi:10.1007/s00382-009-0709-2.

——, ——, and B. Risebrobakken, 2011: Late Eemian warming in the Nordic seas as seen in proxy data and climate models. *Paleoceanography,* **26,** PA2207, doi:10.1029/2010PA002027.

——, T. F. Stocker, C. C. Raible, and A. Levermann, 2012: Is the Atlantic subpolar gyre bistable in comprehensive coupled climate models? *Climate Dyn.,* **40,** 2993–3007, doi:10.1007/s00382-012-1525-7.

——, ——, and A. B. Sandø, 2013: Coupling of eastern and western subpolar North Atlantic: Salt transport in the Irminger Current. *Ocean Sci. Discuss.,* **10,** 555–579, doi:10.5194/osd-10-555-2013.

Colin, C., N. Frank, K. Copard, and E. Douville, 2010: Neodymium isotopic composition of deep-sea corals from the NE Atlantic: Implications for past hydrological changes during the Holocene. *Quat. Sci. Rev.,* **29,** 2509–2517, doi:10.1016/j.quascirev.2010.05.012.

Condron, A., and I. A. Renfrew, 2012: The impact of polar mesoscale storms on northeast Atlantic Ocean circulation. *Nat. Geosci.,* **6,** 34–37, doi:10.1038/ngeo1661.

Curry, R. G., and M. S. McCartney, 2001: Ocean gyre circulation changes associated with the North Atlantic Oscillation. *J. Phys. Oceanogr.,* **31,** 3374–3400.

——, and C. Mauritzen, 2005: Dilution of the northern North Atlantic Ocean in recent decades. *Science,* **308,** 1772–1774.

Delworth, T. L., S. Manabe, and R. J. Stouffer, 1993: Interdecadal variations of the thermohaline circulation in a coupled ocean–atmosphere model. *J. Climate,* **6,** 1993–2011.

Deshayes, J., F. Straneo, and M. A. Spall, 2009: Mechanisms of variability in a convective basin. *J. Mar. Res.,* **67,** 273–303.

Dickson, R. R., and J. Brown, 1994: The production of North Atlantic Deep Water: Sources, rates, and pathways. *J. Geophys. Res.,* **99,** 12 319–12 341.

Dima, M., and G. Lohmann, 2011: Hysteresis behavior of the Atlantic Ocean circulation identified in observational data. *J. Climate,* **24,** 397–403.

Eden, C., and T. Jung, 2001: North Atlantic interdecadal variability: Oceanic response to the North Atlantic Oscillation (1865–1997). *J. Climate,* **14,** 676–691.

——, and J. Willebrand, 2001: Mechanism of interannual to decadal variability of the North Atlantic circulation. *J. Climate,* **14,** 2266–2280.

Gao, Y.-Q., and L. Yu, 2008: Subpolar gyre index and the North Atlantic meridional overturning circulation in a coupled climate model. *Atmos. Oceanic Sci. Lett.,* **1,** 29–32.

Gent, P. R., and Coauthors, 2011: The Community Climate System Model version 4. *J. Climate,* **24,** 4973–4991.

Green, J. S. A., 1970: Transfer properties of the large-scale eddies and the general circulation of the atmosphere. *Quart. J. Roy. Meteor. Soc.,* **96,** 157–185.

Häkkinen, S., and P. B. Rhines, 2004: Decline of subpolar North Atlantic circulation during the 1990s. *Science,* **304,** 555–559.

——, ——, and D. L. Worthen, 2011: Atmospheric blocking and Atlantic multidecadal ocean variability. *Science,* **334,** 655–659, doi:10.1126/science.1205683.

Hátún, H., A. B. Sandø, H. Drange, B. Hansen, and H. Valdimarsson, 2005: Influence of the Atlantic subpolar gyre on the thermohaline circulation. *Science,* **309,** 1841–1844.

Holland, M. M., J. Finnis, and M. C. Serrenze, 2006: Simulated Arctic Ocean freshwater budgets in the twentieth and twenty-first centuries. *J. Climate,* **19,** 6221–6242.

Holliday, N. P., S. Bacon, J. Allen, and E. L. McDonagh, 2009: Circulation and transport in the western boundary currents at Cape Farewell, Greenland. *J. Phys. Oceanogr.,* **39,** 1854–1870.

Iovino, D., F. Straneo, and M. Spall, 2008: The effect of a sill on dense water formation in a marginal sea. *J. Mar. Res.,* **66,** 325–345.

Irvali, N., and Coauthors, 2012: Rapid switches in subpolar North Atlantic hydrography and climate during the last interglacial (MIS 5e). *Paleoceanography,* **27,** PA2207, doi:10.1029/2011PA002244.

Kuhlbrodt, T., S. Titz, U. Feudel, and S. Rahmstorf, 2001: A simple model of seasonal open ocean convection. Part II: Labrador Sea stability and stochastic forcing. *Ocean Dyn.,* **52,** 36–49.

Langehaug, H., I. Medhaug, T. Eldevik, and O. H. Otterå, 2012: Arctic/Atlantic exchanges via the subpolar gyre. *J. Climate,* **25,** 2421–2439.

Latif, M., C. Böning, J. Willebrand, A. Biastoch, J. Dengg, N. Keenlyside, U. Schwenckendiek, and G. Madec, 2006: Is the thermohaline circulation changing? *J. Climate,* **19,** 4631–4637.

Lazier, J. R. N., 1980: Oceanographic conditions at ocean weather ship Bravo, 1964–1974. *Atmos.–Ocean,* **18,** 227–238.

Lehner, F., C. C. Raible, D. Hofer, and T. F. Stocker, 2012: The freshwater balance of polar regions in transient simulations from 1500 to 2100 AD using a comprehensive coupled climate model. *Climate Dyn.,* **39,** 347–363.

Levermann, A., and A. Born, 2007: Bistability of the Atlantic subpolar gyre in a coarse-resolution model. *Geophys. Res. Lett.,* **34,** L24605, doi:10.1029/2007GL031732.

Lohmann, K., H. Drange, and M. Bentsen, 2009a: A possible mechanism for the strong weakening of the North Atlantic subpolar gyre in the mid-1990s. *Geophys. Res. Lett.,* **36,** L15602, doi:10.1029/2009GL039166.

——, ——, and ——, 2009b: Response of the North Atlantic subpolar gyre to persistent North Atlantic Oscillation like forcing. *Climate Dyn.,* **32,** 273–285.

Marotzke, J., 1990: Instabilities and multiple equilibria of the thermohaline circulation. Ph.D. thesis, Christian-Albrechts-Universität Kiel, 127 pp.

——, 2000: Abrupt climate change and thermohaline circulation: Mechanisms and predictability. *Proc. Natl. Acad. Sci. USA,* **97,** 1347–1350.

Marshall, J., and F. Schott, 1999: Open-ocean convection: Observations, theory, and models. *Rev. Geophys.,* **37,** 1–64.

Matei, D., H. Pohlmann, J. Jungclaus, W. Müller, H. Haak, and J. Marotzke, 2012: Two tales of initializing decadal climate prediction experiments with the ECHAM5/MPI-OM model. *J. Climate,* **25,** 8502–8523.

Mellor, G., C. Mechoso, and E. Keto, 1982: A diagnostic calculation of the general circulation of the Atlantic Ocean. *Deep-Sea Res.,* **29,** 1171–1192.

Mengel, M., A. Levermann, C. Schleussner, and A. Born, 2012: Enhanced Atlantic subpolar gyre variability through baroclinic threshold in a coarse resolution model. *Earth Syst. Dyn.,* **3,** 189–197, doi:10.5194/esd-3-189-2012.

Mertz, G., and D. G. Wright, 1992: Interpretations of the JEBAR term. *J. Phys. Oceanogr.,* **22,** 301–305.

Montero-Serrano, J.-C., N. Frank, C. Colin, C. Wienberg, and M. Eisele, 2011: The climate influence on the mid-depth northeast Atlantic gyres viewed by cold-water corals. *Geophys. Res. Lett.,* **38,** L19604, doi:10.1029/2011GL048733.

Montoya, M., A. Griesel, A. Levermann, J. Mignot, M. Hofmann, A. Ganopolski, and S. Rahmstorf, 2005: The earth system model of intermediate complexity CLIMBER-3α. Part I: Description and performance for present-day conditions. *Climate Dyn.,* **25,** 237–263.

——, A. Born, and A. Levermann, 2011: Reversed North Atlantic gyre dynamics in present and glacial climates. *Climate Dyn.,* **36,** 1107–1118, doi:10.1007/s00382-009-0729-y.

Msadek, R., K. W. Dixon, T. L. Delworth, and W. Hurlin, 2010: Assessing the predictability of the Atlantic meridional overturning circulation and associated fingerprints. *Geophys. Res. Lett.,* **37,** L19608, doi:10.1029/2010GL044517.

Myers, P. G., S. A. Josey, B. Wheler, and N. Kulan, 2007: Interdecadal variability in Labrador Sea precipitation minus evaporation and salinity. *Prog. Oceanogr.,* **73,** 341–357.

Rahmstorf, S., 1996: On the freshwater forcing and transport of the Atlantic thermohaline circulation. *Climate Dyn.,* **12,** 799–811.

——, 2001: A simple model of seasonal open ocean convection. Part I: Theory. *Ocean Dyn.,* **52,** 26–35.

Rhein, M., and Coauthors, 2011: Deep water formation, the subpolar gyre, and the meridional overturning circulation in the subpolar North Atlantic. *Deep-Sea Res. II,* **58,** 1819–1832, doi:10.1016/j.dsr2.2010.10.061.

Robson, J., R. Sutton, K. Lohmann, D. Smith, and M. D. Palmer, 2012: Causes of the rapid warming of the North Atlantic Ocean in the mid-1990s. *J. Climate,* **25,** 4116–4134.

Spall, M. A., 2004: Boundary currents and watermass transformation in marginal seas. *J. Phys. Oceanogr.,* **34,** 1197–1213.

——, 2008: Low-frequency interaction between horizontal and overturning gyres in the ocean. *Geophys. Res. Lett.,* **35,** L18614, doi:10.1029/2008GL035206.

——, 2011: On the role of eddies and surface forcing in the heat transport and overturning circulation in marginal seas. *J. Climate,* **24,** 4844–4858.

——, 2012: Influences of precipitation on water mass transformation and deep convection. *J. Phys. Oceanogr.,* **42,** 1684–1700.

——, and D. C. Chapman, 1998: On the efficiency of baroclinic eddy heat transport across narrow fronts. *J. Phys. Oceanogr.,* **28,** 2275–2287.

Stocker, T. F., and D. G. Wright, 1991: Rapid transitions of the ocean's deep circulation induced by changes in surface water fluxes. *Nature,* **351,** 729–732.

Stommel, H., 1961: Thermohaline convection with two stable regimes of flow. *Tellus,* **13,** 224–230.

Stone, P., 1972: A simplified radiative-dynamical model for the static stability of rotating atmospheres. *J. Atmos. Sci.,* **29,** 405–418.

Straneo, F., 2006a: Heat and freshwater transport through the central Labrador Sea. *J. Phys. Oceanogr.,* **36,** 606–628.

——, 2006b: On the connection between dense water formation, overturning, and poleward heat transport in a convective basin. *J. Phys. Oceanogr.,* **36,** 1822–1840.

Swingedouw, D., P. Braconnot, P. Delecluse, E. Guilyardi, and O. Marti, 2007: Quantifying the AMOC feedbacks during a 2×CO_2 stabilization experiment with land-ice melting. *Climate Dyn.,* **29,** 521–534, doi:10.1007/s00382-007-0250-0.

Thornalley, D. J. R., H. Elderfield, and I. N. McCave, 2009: Holocene oscillations in temperature and salinity of the surface North Atlantic. *Nature,* **457,** 711–714.

Treguier, A. M., S. Theetten, E. P. Chassignet, T. Penduff, R. Smith, L. Talley, J. O. Beismann, and C. Böning, 2005: The North Atlantic subpolar gyre in four high-resolution models. *J. Phys. Oceanogr.,* **35,** 757–774.

Tulloch, R., and J. Marshall, 2012: Exploring mechanisms of variability and predictability of Atlantic meridional overturning circulation in two coupled climate models. *J. Climate,* **25,** 4067–4080.

Våge, K., and Coauthors, 2009: Surprising return of deep convection to the subpolar North Atlantic Ocean in winter 2007–2008. *Nat. Geosci.,* **2,** 67–72.

van Aken, H. M., and C. J. de Boer, 1995: On the synoptic hydrography of intermediate and deep water masses in the Iceland Basin. *Deep-Sea Res. I,* **42,** 165–189.

Vellinga, M., and R. A. Wood, 2002: Global climatic impacts of a collapse of the Atlantic thermohaline circulation. *Climatic Change,* **54,** 251–267.

Visbeck, M., J. Marshall, and H. Jones, 1996: Dynamics of isolated convective regions in the ocean. *J. Phys. Oceanogr.,* **26,** 1721–1734.

Walsh, J. E., and D. H. Portis, 1999: Variations of precipitation and evaporation over the North Atlantic Ocean, 1958–1997. *J. Geophys. Res.,* **104** (D14), 16 613–16 631.

Welander, P., 1982: A simple heat–salt oscillator. *Dyn. Atmos. Oceans,* **6,** 233–242, doi:10.1016/0377-0265(82)90030-6.

Yang, D., and O. A. Saenko, 2012: Ocean heat transport and its projected change in CanESM2. *J. Climate,* **25,** 8148–8163.

Yashayaev, I., 2007: Hydrographic changes in the Labrador Sea, 1960–2005. *Prog. Oceanogr.,* **73,** 242–276, doi:10.1016/j.pocean.2007.04.015.

——, and J. W. Loder, 2009: Enhanced production of Labrador Sea water in 2008. *Geophys. Res. Lett.,* **36,** L01606, doi:10.1029/2008GL036162.

Yeager, S., A. Karspeck, G. Danabasoglu, J. Tribbia, and H. Teng, 2012: A decadal prediction case study: Late 20th century North Atlantic Ocean heat content. *J. Climate,* **25,** 5173–5189.

Yoshimori, M., C. C. Raible, T. F. Stocker, and M. Renold, 2010: Simulated decadal oscillations of the Atlantic meridional overturning circulation in a cold climate state. *Climate Dyn.,* **34,** 101–121.